Bioactive Materials 6 (2021) 1452–1463

Contents lists available at ScienceDirect

Bioactive Materials

journal homepage: www.sciencedirect.com/journal/bioactive-materials

Growing vertical aligned mesoporous silica thin film on nanoporous substrate for enhanced degradation, drug delivery and bioactivity

Zhe Li [a,1], Yide He [a,1], Lasse Hyldgaard Klausen [b], Ning Yan [a], Jing Liu [a], Fanghao Chen [a], Wen Song [a,*], Mingdong Dong [b,**], Yumei Zhang [a,***]

[a] State Key Laboratory of Military Stomatology & National Clinical Research Center for Oral Diseases & Shaanxi Key Laboratory of Oral Diseases, Department of Prosthodontics, School of Stomatology, The Fourth Military Medical University, Xi'an, 710032, China
[b] Interdisciplinary Nanoscience Center (iNANO), Aarhus University, Aarhus, 8000, Denmark

ARTICLE INFO

Keywords:
Mesoporous silica film
Vertical aligned mesochannels
Titania nanotubes array
Drug delivery
Osteoblasts

ABSTRACT

Mesoporous silica thin film has been widely used in various fields, particularly the medical implant coating for drug delivery. However, some drawbacks remain with the films produced by traditional method (evaporation-induced self-assembly, EISA), such as the poor permeability caused by their horizontal aligned mesochannels. In this study, the vertical aligned mesoporous silica thin film (VMSTF) is uniformly grown alongside the walls of titania nanotubes array via a biphase stratification growth method, resulting in a hierarchical two-layered nanotubular structure. Due to the exposure of opened mesopores, VMSTF exhibits more appealing performances, including rapid degradation, efficient small-molecular drug (dexamethasone) loading and release, enhanced early adhesion and osteogenic differentiation of MC3T3-E1 cells. This is the first time successfully depositing VMSTF on nanoporous substrate and our findings suggest that the VMSTF may be a promising candidate for bone implant surface coating to obtain bioactive performances.

1. Introduction

Titanium (Ti) has been extensively used in clinic and is considered as an ideal material for bone implant due to its excellent osseointegration capability [1–3]. Unfortunately, the current Ti implant surface is not active enough that a long healing period is required [4]. It is generally accepted that the engineered nanoporous surface is beneficial for osteogenesis [5–7] and our group has devoted tremendous efforts in Ti implant surface biofunctionalization, mainly through the titania nanotubes array fabrication via anodization [8–10]. To further improve TNT surface bioactivity, the surface coating with osteogenic inducers is required. There are three main aspects have to be considered during Ti surface decoration. The first one is the degradation profile of the surface coating. The coating should be disposed in time to allow cell adhesion onto rigid Ti substrate. The second issue is the drug delivery potency of the surface coating. Local delivery of pre-determined drug by the decorated coating is a direct method to biofunctionalize Ti surface [11]. The third important aspect is the bioactivity of the coating material itself. Cytotoxic materials should be avoided and the osteogenic inductive materials may be a rational choice. Therefore, for the biofunctional coating of Ti implant, the decorated coating should be degraded at a proper rate, incorporative for drug package and release, and intrinsic osteoinductive.

Since the discovery of mesoporous silica in early 1990s, it has attracted extensive attentions in biomedical application, due to its well-defined mesopores that are delicately suitable for small molecular drugs storage [12–14]. Moreover, it is also degradable under physiological condition and the product Si element is reported good for osteogensis. Therefore, we suppose that the mesoporous silica may be an ideal material for Ti implant surface coating. There are various different forms

Abbreviations: MSTF, mesoporous silica thin film; VMSTF, vertical aligned MSTF; PMSTF, parallel aligned MSTF; HMSTF, hybrid organic-inorganic MSTF; TNT, titania nanotube; TNN, titania nanonet; HAP, hydroxylapatite nanoparticles; PT, polished titanium; Ti–OH, hydroxylated titanium; DEX, dexamethasone; ALP, alkaline phosphatase; RUNX2, runt-related transcription factor 2; OCN, osteocalcin; OPN, osteopontin.

* Corresponding author.
** Corresponding author.
*** Corresponding author.
E-mail addresses: songwenfmmu@hotmail.com (W. Song), dong@inano.au.dk (M. Dong), wqtzym@fmmu.edu.cn (Y. Zhang).
[1] These authors contributed equally to this work.

https://doi.org/10.1016/j.bioactmat.2020.10.026
Received 16 September 2020; Received in revised form 28 October 2020; Accepted 28 October 2020

such as mesoporous silica nanoparticles, nanorod, and mesoporous silica thin film [15–17]. In fact, there are already number of publications using mesoporous silica nanoparticles for Ti implant surface decoration [18,19]. Although the mesoporous silica nanoparticles are efficient for cell endocytosis, the interaction between nanoparticles and implant surface is vulnerable and the film state may be more suitable for the biomedical devices coating [20]. Unfortunately, the conventional method (evaporation-induced self-assembly) can only obtain parallel aligned mesoporous silica thin film (PMSTF) as surfactant micelles tend to orient horizontal to substrate for reducing the surface energy (Scheme 1a) [21]. This means that the surface of PMSTF is actually a dense silica wall, and the open mesopores are almost invisible, which may limit the performance of mesoporous materials. Actually, nearly all the reported mesoporous silica film deposition on Ti implant surface is fabricated by conventional method and the effect of mesochannels orientation is neglected. For example, Wan et al. encapsulated heparin and vancomycin into mesoporous silicon film, and achieved ideal vascular and antibacterial effects. However, whether the mesochannels orientation will affect the drug release behaviors and biological effects on Ti implant has not been investigated [22].

Recently, the vertical aligned mesoporous silica thin films (VMSTF) has been fabricated, mainly in the areas of catalysis and biosensors [23–25]. Due to the adjustment of the orientation from parallel to vertical, the pores are exposed directly to the external environment (Scheme 1b), which may be more effective for the inner mesochannels exchange. Therefore, the VMSTF may achieve more enhanced bio-performances for Ti implant surface coating. However, whether the VMSTF is applicable in biomedical area has not been investigated. Moreover, all the currently reported protocols of VMSTF is grown on flat surface. The Ti implant surface has to be porous in order to induce osteogenesis. Whether the VMSTF can be deposited on porous Ti implant surface remains unknown yet, considering the fact that the porous surface has significantly reduced the contact area between silica micelles and implant substrate. For creating VMSTF, series of synthesis systems have been established, including self-assembly of ternary surfactant system (C16TMAB–SDS–P123) [26], employment of magnetic fields [27], electro-chemical assistance [28], the Stöber approach [29], and surface modification for confinement effects [30]. The oil-water biphase stratification approach is a newly VMSTF synthesis method without special equipment or complex protocol [31–33].

In this study, the titania nanotubes array (TNT) was fabricated via anodization of pure Ti implant, one of the most extensively studied surface in bone implant decoration [34,35]. The VMSTF was successfully deposited alongside the TNT surface by oil-water biphase stratification method. The VMSTF coated TNT (VMSTF@TNT) showed rapid degradation within several hours, more efficient for dexamethasone loading and significantly enhanced osteoblasts adhesion, proliferation as well as differentiation. These data suggest that the VMSTF is an ideal choice for Ti implant surface coating.

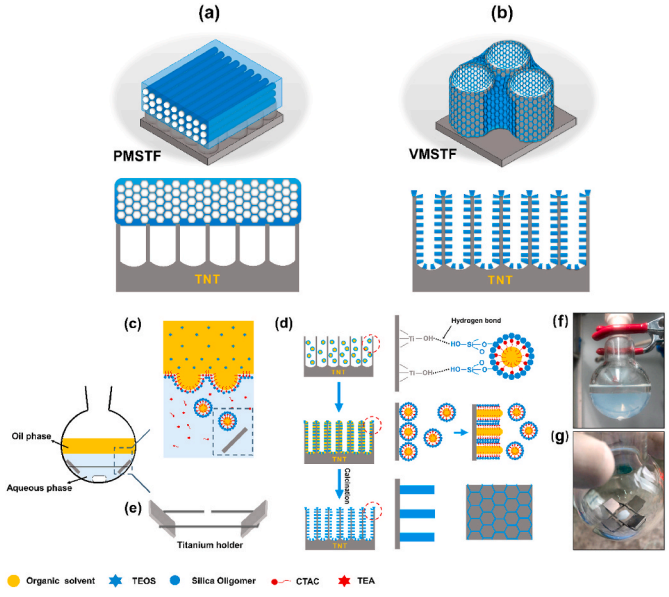

Scheme 1. The structure comparison between conventional PMSTF (a) and VMSTF (b). (c–g) The main steps for the preparation of VMSTF@TNT.

2. Materials and methods

2.1. Materials

Cetyltrimethylammonium chloride (CTAC) (25 wt% in H_2O), hexadecyl trimethyl ammonium bromide (CTAB), triethanolamine (TEA), cyclohexane, decane and dexamethasone (DEX) were purchased from Sigma-Aldrich Corp. Tetraethyl orthosilicate (TEOS), 1,2-bis(triethoxysilyl)ethane (BTSE), phosphate-buffered saline (PBS), cetylpyridinum chloride, and hydroxylapatite nanoparticles (HAP) were purchased from Macklin Corp. Ammonium nitrate (NH_4NO_3) was obtained from Sinopharm Chemical Reagent Co, Ltd. Acetone, ethanol (EtOH), hydrofluoric acid (HF), hydrochloric acid (HCl) were of analytical grade and obtained from Tianjin Fuyu Chemical Co, Ltd. All the above chemicals were used as received without further purification. Hank's Balanced Salt Solution (HBSS) were purchased from Solarbio (Solarbio, China, the components were shown in Table S1). Deionized water was used for all experiments. Pure titanium sheets were purchased from Baoji Titanium Industry Co, Ltd. (Shaanxi, China). These substrates were firstly burnished from 240# to 7000# with waterproof SiC sandpaper and ultrasonic cleaning by acetone, ethanol, deionized water, respectively. Then, they were stored in ethanol for subsequent experiments and some of them also served as polished titanium (PT). 1 cm × 1 cm square titanium sheet was used for characterization, round sheets with 1.5 cm diameter were used for drug delivery and cell experiments considering they can perfect fit with 24-well plates.

2.2. Measurements and characterization

Field emission scanning electron microscopy (FE-SEM) images were taken on a Hitachi S-4800 microscope operating at 20 kV. The surface topography and roughness were determined by atomic force microscope (AFM; Shimadzu, Tokyo, Japan). Field emission transmission electron microscopy (FE-TEM) experiments were conducted on a JEOL JEM–F200 microscope (Japan) operated at 200 kV. The samples for the FE-TEM measurements were suspended in ethanol and supported onto a holey carbon membrane on a Cu grid. Infrared spectra of the VMSTF and dexamethasone were collected using a Nicolet 6700 Fourier transform infrared (FTIR) spectrophotometer (Thermo Scientific, Waltham, MA, USA) equipped with an attenuated total reflection (ATR) setup. Infrared spectra between 2000 and 400 cm^{-1} at 4 cm^{-1} resolution were collected using 32 scans. The accumulated Si release concentration was determined by inductively coupled plasma-atomic emission spectroscopy (ICP-AES, PE5300DV, Spectro Genesis, Germany). The silanol groups (Si–OH) in VMSTF were tested by high-resolution solid-state ^{29}Si NMR spectroscopy (Burker 400 M) in single pulse mode. The ions concentrations absorbed from HBSS (Na^+, K^+, Ca^{2+}, Mg^{2+}) were determined by inductively coupled plasma mass spectrometer (ICP-MS, NexIONTM 350D, PerkinElmer, USA). The water contact angle was measured by the DSA1 System (Krüss, Hamburg, Germany). Pore size distribution was analyzed by measuring represented FE-SEM or FE-TEM images with ImageJ software (NIH, USA) and test the goodness of fit of a Gaussian distribution by Origin 2018 (OriginLab Cooperation, North hampton, MA, USA). R^2 represent adjusted R^2 value. The diameter distributions of BSA in different solution were observed by dynamic light scattering (DLS) measurements using a Malvern Zetasizer (Malvern Instruments, UK).

2.3. Preparation of vertical aligned mesoporous silica thin film

The vertical aligned mesoporous silica thin film (VMSTF) was fabricated according to Liu's report [30]. Briefly, 7.5 mL of CTAC solution (25 wt%), 0.09 mL of TEA, 17.5 mL of deionized water were mix together. Then, the TNT was held by pre-twisted pure titanium wires and put into a 50-mL round bottom flask. Then, the mixture above (pH of 10) was transferred to the flask and stirred gently (450 rpm) at 60 °C for 1 h. 8.5 mL of a solution of TEOS in cyclohexane (15% v/v) was carefully added into the above mixture dropwise at 60 °C. Reaction was continued at a constant temperature with continuous stirring for a certain time. The TNT was taken out, and washed with deionized water and ethanol, and then dried at 60 °C for 1 h. After removing the surfactant template by simple calcination at 500 °C for 3 h in air, the VMSTF@TNT was obtained. By altering the TNT to titania nanonet (TNN) or hydroxyapatite nanoparticle (HAP), we can also fabricate VMSTF@TNN and VMSTF@HAP. TNN was fabricated by immersing TNT with diameter of 100 nm into NaOH solution (2 M) at room temperature for 2 h.

2.4. Preparation of organic-inorganic hybrid mesoporous silica thin films

Typical synthesis of the hybrid mesoporous organic-inorganic silica thin film (HMSTF) was performed as follow [36]. 60 mg of CTAB and 250 μL of NaOH (0.1 M) were added in 30 mL of deionized water. Then TNT with titanium holder was put in the round bottom flask. After stirring for 1 h at room temperature, 3 mL of cyclohexane containing 40 μL of silane precursors (V_{BTSE}/V_{TEOS} = 1/0, 3/1, 1/1, 1/3) was added dropwise and continued to react for another 4 h. Finally, the obtained product was washed three times with water, and immersed in 50 mL of NH_4NO_3 ethanol solution (0.2 wt%) and heated at 60 °C for 2 h to remove the template CTAB. This step was repeated for 3 times and HMSTF@TNT was obtained.

2.5. Preparation of parallel aligned mesoporous silica thin film

Parallel aligned mesoporous silica thin film (PMSTF) was obtained by traditional evaporation-induced self-assembly method [37]. In brief, TEOS, ethanol, deionized water and dilute HCl (0.1 M) were refluxed at 80 °C for 90 min. Then, CTAB was dissolved in ethanol and added to the prehydrolysed solution together with an additional amount of water and HCl (pH = 2). The final reactant molar ratio was 1 TEOS: 22 EtOH: 0.004 HCl: $5H_2O$: 0.096 CTAB. After aging for 2 d at room temperature, the dip-coating procedure was performed on TNT at a withdrawal speed of 75 mm/min and as-deposited thin film was heat-treated in air at 150 °C for 12 h to dry and complete siloxane condensation. Finally, PMSTF was obtained by calcination at 500 °C for 3 h.

2.6. In vitro degradation

The degradation experiments in vitro were carried out by immersing VMSTF@TNT (3 replicates) into 1 mL of PBS in 24-well plate at constant temperature of 37 °C and shaking rate of 100 rpm. The sample solutions were completely collected at different time points and then another 1 mL of fresh PBS was added. The accumulated concentrations of free silicon were determined using an inductively coupled plasma atomic emission spectrometer (ICP-AES). Meanwhile, in order to determine whether the degradation product is water-soluble silicates or structured debris, the soaking solutions were collected for FE-TEM observation.

2.7. Dexamethasone loading and releasing

All samples were put in 24-well plate with 1 mL of dexamethasone (DEX) ethanol solution (10 mg/mL). After 4 h impregnation by the usage of vacuum pumping, all samples were washed twice with deionized water and dried in vacuum to obtain DEX loaded samples. The loaded amount of DEX was calculated by determining the difference of DEX concentration before and after loading. The concentrations of DEX were measured by the absorbance value at 242 nm with a 96-well UV transparent microplate (Corning, Item No. 3635) by microplate reader (Biotek Epoch, USA) and analyzed by Gen 5 Software (BioTek Instruments, Winooski, VT). The standard curve of DEX solution was shown in Fig. S1.

The release profiles of DEX loaded samples were tested in 5 mL of PBS solution (0.01 M, pH7.4) under 37 °C. 100 μL supernatant was collected at each time points and another 100 μL fresh PBS solution was added. The accumulative release rate of DEX (%) was calculated with the following equation: DEX (%) = (total amount of DEX released)/(total loading amount).

2.8. Cell culture and sample preparation

MC3T3-E1 pre-osteoblast cells (CRL-2593, ATCC, Manassas, VA, USA) were cultured in α-modified minimal essential medium (α-MEM, Gibco, USA) with 10% bovine calf serum (BCS, Sijiqing Company, Hangzhou) and 1% penicillin/streptomycin (Sigma, USA) and incubated in a humidified atmosphere of 5% CO2 at 37 °C. All control groups (PT, TNT) were annealed together with VMSTF@TNT to avoid the bias of crystals of substrates on cell behaviors That was why these substrates exhibited different appearances. All samples were sterilized with 75% ethanol for 2 h and irradiated by UV light for 30 min before seeding.

2.9. Immunofluorescence staining

MC3T3-E1 cells were seeded on the samples in 24-well plate (Corning, USA) at the density of 5×10^4 cells/well, after incubating for 2 h, the cells were washed three times with PBS and then fixed with 4% paraformaldehyde (Feiyang Biotechnology Co, Ltd, Shaanxi, China) for 15 min. The actin filaments of MC3T3-E1 cells were stained with Alexa Fluor 488 phalloidin (Invitrogen) for 1 h, and Hoechst 33258 (Sigma) was used for staining the nucleus for 10 min. After mounting, the samples were observed using confocal laser scanning microscopy (CLSM) (Nikon, A1 PLUS, Tokyo, Japan). Cell attachment amount was calculated by ImageJ software. The vinculin staining was performed after incubating for 24 h. The additional steps are as follows. Briefly, after fixing with 4% paraformaldehyde, cells were permeabilized and blocked with 0.2% Triton X-100 (Sigma) and normal Goat Serum (Ready-to-use, Boster Biological Technology, Ltd, Wuhan, China) for 10 min and 30 min, respectively. Then, they were incubated with primary antibodies (Vinculin Recombinant Rabbit Monoclonal Antibody (42H89L44), Invitrogen) overnight at 4 °C and goat anti-rabbit IgG atto 594 was used as secondary antibodies for another 2 h at room temperature.

2.10. Cell viability

Cell viability was quantified by the Cell Counting Kit-8 (CCK-8, Dojindo, Kumamoto, Japan) at 24, 72 h after seeding on samples in 24-well plate at the density of 6×10^4 cells/well. The cell culture medium was replaced with fresh medium containing 10% CCK-8. After 3 h incubation in an incubator, 100 μL of the medium was transferred to a 96-well plate and the absorbance of the solutions was measured at 450 nm using a microplate reader.

2.11. Osteogenic related genes expression

1×10^5 cells were seeded on the samples and cultured for 24 h. Following this, the medium was replaced with osteogenic differentiation medium (ODM) consisting of α-MEM supplemented with 50 mM L-ascorbic acid, 10 mM β-glycerophosphate, and 1 nM dexamethasone. The ODM was changed every day throughout the experiments. The expression of osteogenesis related genes was evaluated using the real-time polymerase chain reaction (q-PCR). The cells were cultured in ODM for 3 and 7 days. The total RNA was isolated using the RNAiso Plus (TaKaRa) according to the manufacturer's instructions. 1 mg RNA from

each sample was reversed transcribed into complementary DNA (cDNA) using the PrimeScript RT reagent kit (TaKaRa). Relative mRNA expression levels were quantified using Real-time PCR (Bio-Rad iQ5 Multicolor Real-Time PCR Detection System) with TB Green® Premix Ex Taq™ II (TaKaRa). The q-PCR process contained a start at 95 °C for 30 s, followed by 40 cycles of 95 °C for 5 s and 60 °C for 30 s. Data analysis was carried out using the iQTM5 Optical System Software Version 2.0 (Bio-Rad). The relative expression levels for osteogenesis related genes including alkaline phosphatase (ALP), runt-related transcription factor 2 (RUNX2), osteocalcin (OCN) and osteopontin (OPN) were normalized to the housekeeping gene, Glyceraldehyde 3-phosphate dehydrogenase (GAPDH). The forward and reverse primers for the selected genes were list in Table S2.

2.12. Intracellular total protein isolation and alkaline phosphatase activity

After 7 days of culturing in ODM, the cells were washed three times with PBS and treated with 0.1% Triton X-100 (Solarbio, China) through three standard freeze thaw cycles. The ALP activities of the samples were determined by a colorimetric assay using an ALP reagent (Beyotime Institute of Biotechnology) containing p-nitrophenyl phosphate (p-NPP) as the substrate. The absorbance of p-nitrophenol formed was measured at a wavelength of 405 nm. The intracellular total protein content was determined using the MicroBCA protein assay kit (Thermo Scientific) (Fig. S2), and the ALP activity was normalized to the total protein content.

2.13. Alkaline phosphatase staining

After culturing MC3T3-E1 cells in the ODM for 7 d, all samples were rinsed with PBS, fixed with 4% paraformaldehyde for 15 min, and then washed twice with PBS. ALP activity was stained for 20 min by using a BCIP/NBT alkaline phosphatase color development kit (Beyotime Institute of Biotechnology) and imaged with a digital camera.

2.14. Alizarin Red staining

After culturing for 21 days in ODM, the cells were washed thrice with PBS and fixed in 60% isopropyl alcohol for 5 min. Followed by washing twice with deionized water. All samples were stained with 1% Alizarin Red (Sigma-Aldrich) in deionized water for 3 min at room temperature. After rinsing with deionized water, images were acquired. In the quantitative analysis, the stain was dissolved in 1 mL of 10% cetylpyridinum chloride aqueous solution and the absorbance values were measured at 540 nm.

2.15. Absorption of bovine serum albumin and FITC labeled bovine serum albumin

Before testing, all samples were store in the oven at 60 °C overnight for completely drying. Then, they were put in 24-well plate with 400 μL of bovine serum albumin (BSA) dissolved in deionized water or HBSS (1 mg/mL). Next, the test was performed at room temperature with a shaker (80 rpm). 2 μl of supernatant will be carefully collected and quantified with Micro BCA™ Protein Assay Kit (Thermo Scientific). The standard curve of BSA solution was shown in Fig. S3. At the same time, FITC-BSA (Solarbio) was dissolved in HBSS with same concentration (1 mg/mL), all sample were soaked for 4 h and observed by CLSM.

2.16. Cell sample preparation for FE-SEM

After culturing for 24 h, all samples were rinsed with PBS for three times to remove the floating cells. Next, they were fixed with 2.5% glutaraldehyde overnight at 4 °C, dehydrated in a graded series of ethanol (30, 50, 70, 80, 90, 100%), then dried with hexamethyldisilazane (HMDS) for 30 min, and started spraying platinum.

2.17. Determination of cell adhesion force and confocal mosaic technology

Cell adhesion force is tested by centrifugation referring to the previously reported method [38,39]. In brief, all samples were firstly rinsed with PBS for removing the floating cells at 24 h after culturing. Subsequently, the samples were placed upside down at the bottom of 50 mL centrifuge tubes and incubated with PBS. After being centrifuged respectively at 600 and 1300 rpm for 5 min. Then, the remaining cells and the cells without centrifugation were stained by Hoechst. Considering the attached cells are not evenly distributed, so the cells on entire samples (with a diameter of 15 mm) were observed by confocal mosaic technology for the accuracy of the test. That means each confocal mosaic image is stitched together from 100 to 120 partial images. All processes are automatically completed by Nikon confocal laser microscope (Nikon, A1 PLUS, Tokyo, Japan). Next, the cells were calculated by ImageJ and the force exerted on each cell (f) was calculated referring to the following equation [38]:

$$f = (\rho_{cell} - \rho_{PBS}) \times V_{cell} \times \omega^2 \times r$$

Here, $\rho_{cell}$and $\rho_{PBS}$are the density of cells (about 1.07 g/cm^3) and PBS (about 1.01 g/cm^3), respectively. V_{cell}represents the cell volume of MC3T3-E1 and is about 3000 μm^3 [40]. $\omega$is the centrifugation angular velocity, and $r$is the distance of the sample to the rotation center. We assumed that the distribution of cell adhesion force obeys normal distribution [38]:

$$f \sim N(\mu, \sigma^2)$$

Here, $\mu$is the mean cell adhesion force and σ is the standard deviation. Therefore, the mean value of the cell adhesion force (μ) could be figured out according to the standard normal distribution [38]:

$$\frac{f-\mu}{\sigma} \sim N(0,1)$$

2.18. Statistical analysis

At least 3 samples per group were tested for each experiment and presented as mean ± standard deviation. The statistical analysis was performed using one-way ANOVA by GraphPad Prism software. The $p < 0.05$ was considered significance and $p < 0.01$ was considered strong significance.

3. Results and discussion

3.1. Preparation of VMSTF@TNT

The fabrication of hierarchical VMSTF@TNT was illustrated in Scheme 1c-g. The conventional EISA method is usually performed via a sol-gel process in precursor solution, so that the film is impossible to penetrate and disperse uniformly into the narrow interior space of nanotopography. However, the VMSTF fabricated in this study is a novel biphase stratification growth way. Such facile biphase synthesis system not only enables the slowly and uniformly self-assembly at the interface between organic surfactants and inorganic silica oligomers [41,42], the introducing of oil phase may also orientate the growth direction of mesochannels [21]. Specifically, the biphase system consisted of an oil phase containing tetraethyl orthosilicate (TEOS) as silicon source, and an aqueous phase containing cetyltrimethylammonium chloride (CTAC) as the template. As the micelles continually form at the oil-water interface, they become spherical and slowly drive into the lower phase to obtain the minimum interface energy (Scheme 1c) [33]. With a gentle stirring, the tiny micelles disperse uniformly, then penetrate and deposit

on the surface of nanotubes by hydrogen bond. Meanwhile, the typical Tyndall effect in aqueous solution can be seen as reaction proceed (Scheme 1f). The deposited spherical micelles will form an ordered mesoporous array to reduce the surface energy. Finally, the VMSTF is obtained after removal of template by calcination (Scheme 1d). Pure titanium wires were twisted as the holders (Scheme 1e, g), in order to produce more samples in one reaction cycle to satisfy the following experiments.

3.2. Observations of VMSTFs growing on TNTs with different diameters

Prior to our study, TNTs with diameters ranging from 15 nm to 100 nm (Fig. 1 a-e) were prepared to validate the critical discontinuity that hamper VMSTFs growth. To our surprise, VMSTFs were successfully deposited on all TNTs after reacting for 4 h (Fig. 1 f-o). It may be attributed to the biphase system, which make it possible to maintain a gentle growth rate and form permeable tiny micelles [41,42]. In addition, the mesostructures were also similar, indicating that the TNTs did not hamper the formation of VMSTFs. However, the VMSTFs were thicker and the substrate nanotubes were invisible when the diameter was less than 50 nm. This may because that the micelles are able to cover directly on smaller nanotubes whereas they can only deposit on the walls of larger tubes. On the other hand, we hydroxylated the polished smooth titanium sheet (Ti–OH) by mild alkaline treatment (0.05 M NaOH treated for 3 min) [43], without creating certain surface morphology. The data indicated that VMSTFs could successfully grow on Ti–OH, but failed on the untreated polished titanium (PT, Fig. S4). Taken together, these findings support that the hydroxyl group of the substrate surface is the key to VMSTFs synthesis, as mentioned in the previous literatures that the strong van der Waals force between hydroxyl groups of substrates and silica micelles initiates the VMSTFs growth [33]. According to this theory, VMSTFs were also successfully synthesized on other substrates in this study, including titania nanonets and hydroxyapatite nanoparticles (Fig. S5). In order to create VMSTFs without losing the substrate nanotubes signature, the TNT with the larger diameter of 100 nm was used in the subsequent analysis, unless specifically mentioned.

3.3. Dynamic of mesopore diameter in different synthetic conditions

The pore diameter of the VMSTFs is very important for their performance [44]. Many researches have found that the pore size of VMSTFs is tunable by changing the molecular weight of organic solvents and/or silicon source (TEOS) proportion in the biphase system [45,46]. Considering this, a comparative study was performed by using different organic solvents of cyclohexane (Mw = 84) and decane (Mw = 142) and volume ratios of TEOS (5%, 15%, 30%) (Fig. 2). Controversial to existing

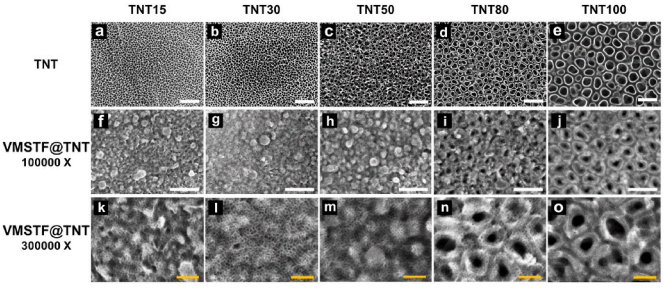

Fig. 1. The TNT was fabricated by anodization of pure titanium in HF, under different voltages to obtain various pore diameters of 15 nm (TNT15), 30 nm (TNT30), 50 nm (TNT50), 80 nm (TNT80), and 100 nm (TNT100) respectively (a–e). (f–o) The surface morphology observation after VMSTF growth on TNT surface. White scale bar = 200 nm, yellow scale bar = 50 nm. (For interpretation of the references to color in this figure legend, the reader is referred to the Web version of this article.)

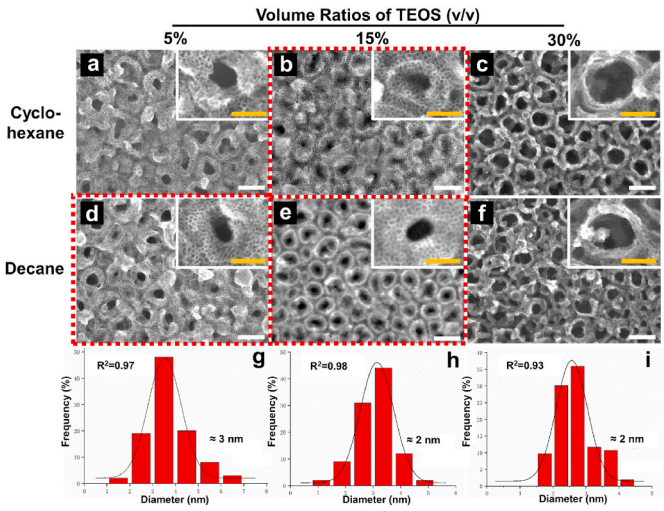

Fig. 2. The morphology of VMSTFs on TNT100 surface under different combinations of organic solvents and silicon source ratios (a–f). The pore size distributions of b, d, and e respectively that quantified by ImageJ software (g–i). White scale bar = 100 nm, yellow scale bar = 50 nm. (For interpretation of the references to color in this figure legend, the reader is referred to the Web version of this article.)

reports, only the combinations of cyclohexane + TEOS15% (Fig. 2b), decane + TEOS5% (Fig. 2d), and decane + TEOS15% (Fig. 2e), could obtain regular mesopores. Moreover, the pore sizes distributions finely fit the Gaussian distribution ($R^2 > 0.9$), with similar average sizes of ~3 nm. Our findings indicated that the organic solvent and TEOS ratio are strictly limited when growing VMSTF on a discontinuous substrate, and the pore size is relatively stable. This may possibly due to the substrate discontinuity that has influenced the interaction with micelles, but the exact mechanisms still need further elucidation. This result suggests that our fabrication strategy is technical insensitive, and a reproducible mesostructure can be formed in different synthetic conditions. In the following examination, the VMSTFs were fabricated in cyclohexane + TEOS15%, in order to obtain a relative larger mesopore size.

3.4. Characterization of VMSTF@TNT

Then the in situ growing process was recorded in detail (Fig. 3). According to the top view of FE-SEM images (Fig. 3a), a small amount of unstructured tenuous substances began to grow on the surface of TNTs as early as 1 h post reaction. When the reaction proceeded for 2 h, a thin layer of VMSTF appeared for the first time, and became more obvious at 4 h. Then, the substrate nanotubes were gradually filled by VMSTF, until 24 h that the TNTs were completely covered by VMSTF. By cross-section of the sample, the VMSTF was also uniformly deposited inside of the nanotubes (Fig. 3b). Meanwhile, the AFM scanning was performed after 0, 2, 4 and 24 h post deposition and the related Sq roughness was calculated (Fig. 3c and d). It was notable that the surface topography and related Sq roughness did not changed obviously before 4 h. However, when the reaction proceeded to 24 h, the topography was significantly changed and the Sq roughness increased to ~32 nm. This process is consistent with FE-SEM observation, suggesting that VMSTF is mainly deposited inside TNT in the early stage, and will completely cover TNT afterwards, resulting in a "vertical mesoporous silica on vertical nanotubes structure" (Fig. 3e).

Then, the FE-TEM was performed to observe the more detailed structure. The images showed that the VMSTF was uniform and flawless, which closely interacted with both the inner and inter surfaces of TNT walls (Fig. 4a and b). The higher magnification image in STEM mode showed clearly the "nanoring-like" structure of VMSTF@TNT, and the thickness of VMSTF is about 20 nm (Inset of Fig. 4b). The EDS mapping

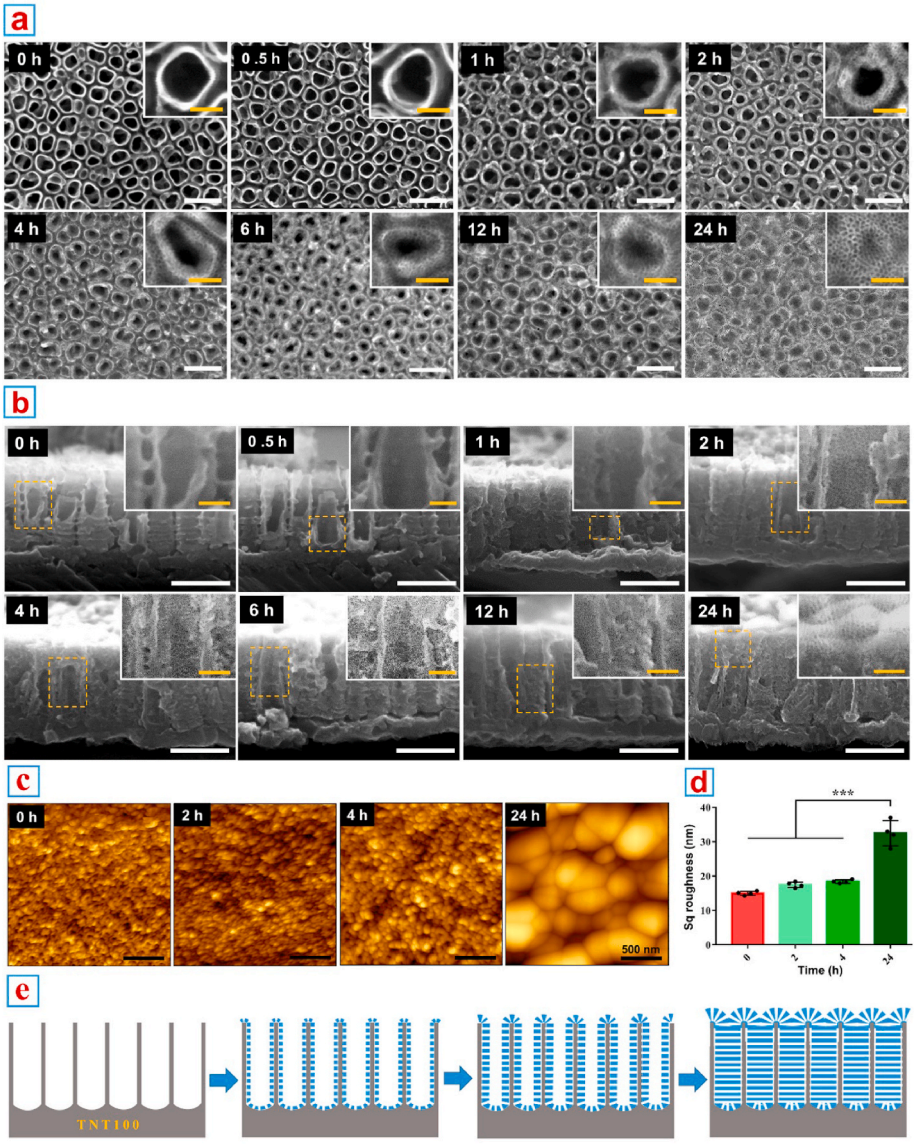

Fig. 3. In situ growing process of VMSTF@TNT. (a, b) FE-SEM observations of the VMSTFs growing in different time points from the top and lateral view. (c, d) The AFM scanning images and Sq roughness calculation. (e) The illustrations depict the growth process of VMSTF@TNT. White scale bar = 200 nm, yellow scale bar = 50 nm ***$p < 0.01$. (For interpretation of the references to color in this figure legend, the reader is referred to the Web version of this article.)

clearly showed that the titanium (Ti) element composed the wall of the TNT, while oxygen (O) and silicon (Si) were enriched adjacent to the wall (Fig. 4c and d). The ATR-FTIR spectroscopy confirmed the peaks at 1080 cm^{-1}, 793 cm^{-1}, and 473 cm^{-1} (Fig. 4e), which corresponded to antisymmetric stretching, symmetric stretching and bending vibration mode of Si–O–Si bond respectively [47,48]. The peak at 950 cm^{-1} was attributed to the stretching vibration of Si–OH group [49]. Taken together, these characterizations directly illustrated the formulation of two-layered nanotubular structures of VMSTF@TNT. Unfortunately, other characterization methods that commonly used, like GISAXS, N_2 adsorption and desorption analysis, seemed not applicable to this study, due to the interference from titania nanotubes.

3.5. Biodegradability

Biodegradability is always the primary consideration for implant materials. It has been reported that the degradation process of mesoporous silica nanoparticles will last one or two weeks, which may cause potential toxicity due to the long exposure to high dose of nanoparticles [50–52]. Therefore, the fast degradability of VMSTF is of crucial important to ensure safety. First, the accumulated Si release concentration was analyzed by ICP-AES in a simulated physiological environment in three days (Fig. 5a). The released Si concentration increased rapidly in the initial stage and reached the plateau phase after 24 h. The FE-SEM examination indicated that the mesostructure was only visible within 2 h incubation, whereas the structure disintegrated quickly afterwards and was almost completely invisible at 24 h (Fig. 5b). In addition, the degraded products were collected to perform TEM observation. There was no apparent mesostructural fragments of silica film, suggesting that the mesochannels were destroyed in aqueous condition (Fig. S6). The degradation of mesoporous silica is mainly attributed to the active silanol groups (Si–OH) on film surface. It was reported that Si–OH groups are enriched inside the mesopores, and are easily attacked by OH- in water, causing the destruction of Si–O–Si bond and the collapse of mesostructure [36,50]. In this study, the Si–OH groups were still exist in VMSTF after calcination (Fig. S7) with the content of 5.56 wt % (Table S3). Moreover, they are more convenient for substances exchange with the external environment, which may be the main reason for rapid degradability. On the other hand, the degradability of VMSTF is also tunable by reducing Si–OH number, such as hybridizing the silica

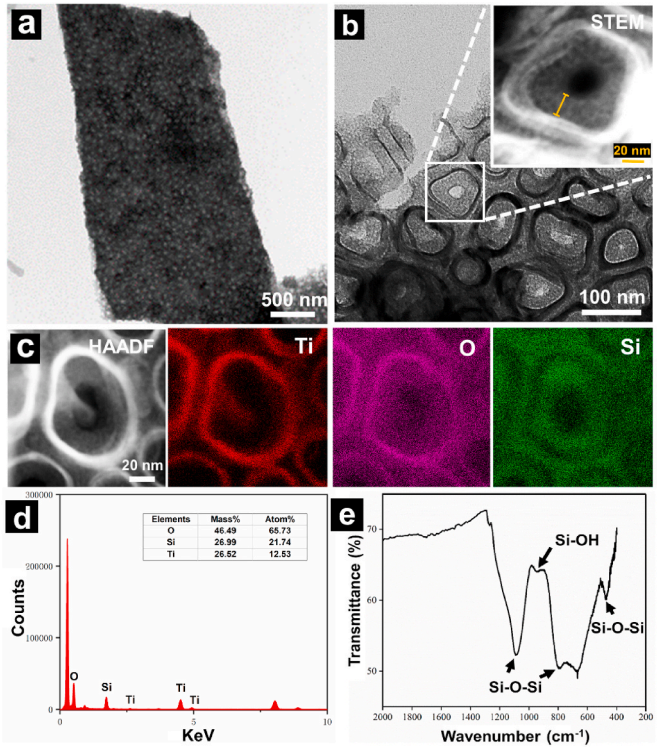

Fig. 4. FE-TEM (a, b), STEM (inset), EDS mapping (c) with element analysis (d) and ATR-FTIR spectrum (e) of the VMSTF on TNT100.

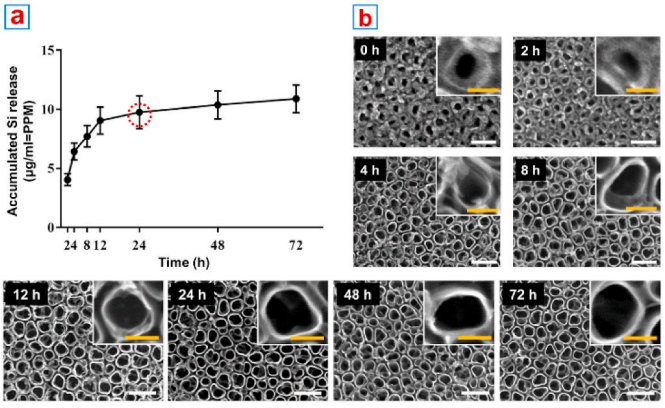

Fig. 5. ICP-AES analysis of the released silicon ion (a) and the FE-SEM observations of VMSTF@TNT after incubation with PBS for 72 h (b). White scale bar = 200 nm, yellow scale bar = 50 nm. (For interpretation of the references to color in this figure legend, the reader is referred to the Web version of this article.)

sources with organic composition (Fig. S8) [53,54]. Anyway, the fast degradation of VMSTF is very attractive as a biomaterial coating. Not only it can be more reliable for biosafety, the potential harm caused by the collapse of coating can also be avoided and the cells can attach on rigid titanium implant surface in time [55].

3.6. Drug loading and release properties

To demonstrate the capability of vertical aligned VMSTF in drug delivery, the DEX was chosen as a guest molecule, which was extensively used as a small molecular drug for enhancing proliferation and differentiation of osteoblasts [56,57]. At the same time, the PMSTF was also prepared on the TNT surface by traditional evaporation-induced self-assembly (EISA) method (Fig. S9). After DEX adsorption, the surfaces of TNT and PMSTF were partially covered, while the VMSTF@TNT were almost fully occupied (Fig. 6a). The presence of DEX was further verified by ATR-FTIR (Fig. 6b) that the stretching vibration at 1702 cm^{-1}, 1662 cm^{-1}, 1620 cm^{-1} were observed due to C = O and C = C (in ring) double bond framework conjugated to C = O bonds from the DEX immobilization [58]. The loading quantification (Fig. 6c) indicated that the VMSTF was significantly higher than TNT and PMSTF (1.73 mg/cm^2, 0.76 mg/cm^2, and 0.71 mg/cm^2, respectively). This suggests that vertical aligned mesoporous film is more efficient in cargo package. Next, the DEX release style was evaluated in a simulated physiological environment (PBS, PH = 7.4, 37 °C). All the three surfaces showed a burst release that more than 80% DEX was released within several hours (Fig. 6d). Nevertheless, the DEX from VMSTF@TNT was released a little bit slower than TNT and PMSTF, which might because that the DEX penetrated into the inner part of mesochannels on VMSTF surface. In this part, we have preliminary demonstrated that the vertical aligned mesochannels are more efficient of carrying small molecular drug compared to conventional horizontal aligned mesochannels. But the further post-modification may be required to achieve a sustained or controlled release performance.

3.7. Hydrophilicity and cell behaviors

The hydrophilicity of implant surface is closely related to the early biological behavior of osteoblasts [59]. In our study, VMSTF@TNT showed a hydrophilic surface that when the water droplet attached the substrate, it spreaded the entire surface immediately (Fig. 7a). This may be attributed to the numerous exposed mesopores with plenty of hydroxyl groups. When the hydroxyl groups are reduced by organic silica hybridizing, the surface water contact angle is also increased (Fig. S10a). Then the MC3T3-E1 cells were used to evaluate the cell behaviors on the VMSTF@TNT considering they are widely used models to evaluate the performances of biomaterial. After adhesion for 2 h, the attached cell number on VMSTF@TNT surface was significantly higher than PT and TNT (Fig. 7b and c). In addition, the cells were stretched more obviously with numerous filopodia, while the cells on the surface of PT and TNT were almost round shape with few filopodia (Fig. 7d).

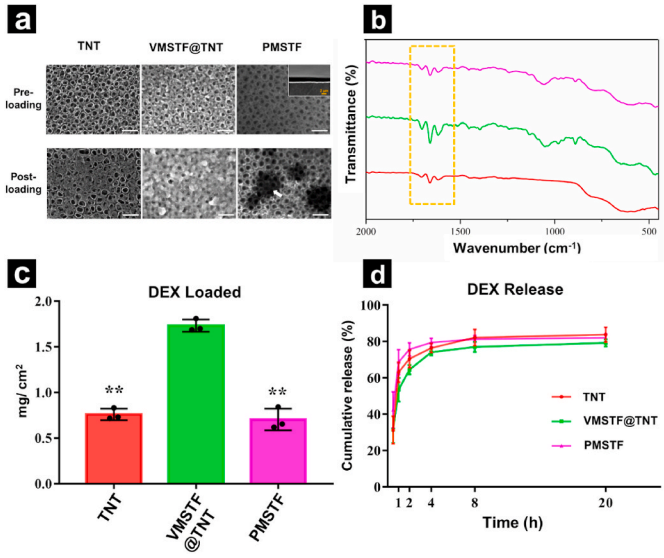

Fig. 6. Drug delivery from different surfaces. (a) DEX loading observation by FE-SEM. White scale bar = 200 nm, yellow scale bar = 50 nm. (b) ATR-FTIR spectrum of DEX loaded samples and (c, d) their DEX loading/release behaviors. *p < 0.05, **p < 0.01 (vs VMSTF@TNT). (For interpretation of the references to color in this figure legend, the reader is referred to the Web version of this article.)

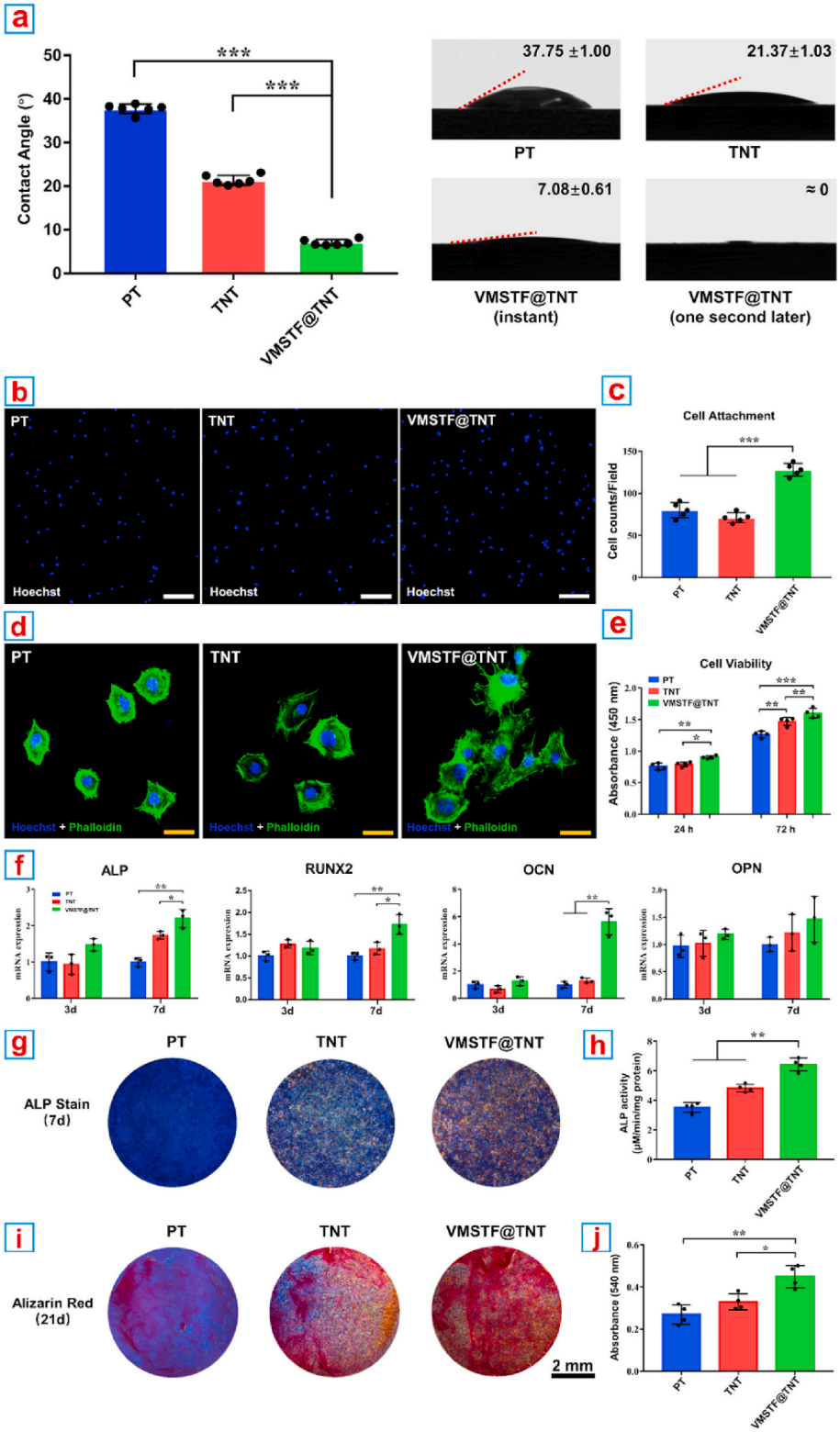

Fig. 7. Hydrophilicity, cell behaviors and osteogenic differentiation on the surface of three samples. (a) Water contact angle measurements. (b, c) CLSM images showing the attachment and morphology of MC3T3-E1. White scale bar = 200 nm, yellow scale bar = 50 nm, blue bar = 5 μm. (d) Quantification of attached cell counts. (e) Cell viability of MC3T3-E1 as measured by CCK-8. (f) Relative mRNA expression of four osteogenic genes. (g, h) The ALP activity staining and quantification. (i, j) The calcium nodules formation evaluation by Alizarin Red staining and semi-quantification. *p < 0.05, **p < 0.01, ***p < 0.001. (For interpretation of the references to color in this figure legend, the reader is referred to the Web version of this article.)

Next, the cell viability was evaluated by CCK-8 test after cultivation for 24 h and 72 h, respectively (Fig. 7e). Generally, the cell viability was increased at 72 h compared to 24 h in all the groups, indicating that the cells were proliferated normally. It was notable that the cell viability was the highest on VMSTF@TNT surface all the time, suggesting a positive effect of VMSTF for cell proliferation. Finally, a serial typical assays were performed to evaluate the osteogenic differentiation of MC3T3-E1 on VMSTF@TNT. The expression of osteogenic genes including ALP, RUNX2, OCN, OPN were significantly enhanced on VMSTF@TNT after induction for 7 days (Fig. 7f). The ALP activity and mineralization on the VMSTF@TNT surface were also significantly enhanced (Fig. 7g–j). These results confirm that VMSTF could play a positive role in all stages of osteoblast functions, which is very attractive for orthopedic implant surface decoration.

3.8. Primary exploration of the enhanced cell adhesion

How the VMSTF enhanced the cell adhesion has aroused our great interest. Dozens of literatures have reported that the protein adsorption capacity of the biomaterial surface will directly affect the cell adhesion behavior [60,61]. Therefore, BSA (Bovine Serum Albumin), the most common soluble protein in serum. was served as a model in this study. When all samples were tested in BSA aqueous solution (deionized water), TNT appeared the highest protein adsorption capacity, while VMSTF@TNT and PMSTF were both lower (Fig. 8a left). This may be due to the fact that the size of nanotube (~100 nm) was enough big to contain more BSA, compared with mesopores (~4 nm). To our surprise, when the BSA in HBSS solution (Hanks Balanced Salt Solutions with calcium, magnesium) was used, the result was reversed, VMSTF@TNT exhibited the strongest adsorption capacity (Fig. 8a middle), and this result was further confirmed by the absorption of FITC-BSA for 4 h (Fig. 8b). It proves that some ions contained in HBSS played a decisive role in BSA absorption process. Next, all samples were pre-soaked in pure HBSS and then tested in BSA aqueous solution. We found that the adsorption capacity of VMSTF@TNT was significantly improved in the early stage, but fall back to the same level with TNT in the end (Fig. 8a right). This suggests that in HBSS, which is more similar to the physiological environment, there may exist two simultaneous processes in the adsorption of BSA on VMSTF@TNT. On the one hand, the surface charge distribution of VMSTF@TNT may be changed in a short time through absorbing some cations via Si–OH group, causing a rapid promotion in BSA adsorption. On the other hand, which may be a more important process, BSA may interact with certain cations in HBSS, and these cations served as bridges to introduce BSA to the surface of VMSTF. Therefore, we further used ICP-MS to evaluate the cations adsorption quantity from HBSS, and the results showed that VMSTF@TNT showed a stronger adsorption capacity for Na^+ and Ca^{2+} (Fig. 8c). Numerous studies have shown that in a neutral environment, silanol groups can adsorb Na^+ and Ca^{2+} to form surface coordination compounds, instead of precipitation. The possible reactions are as follows:

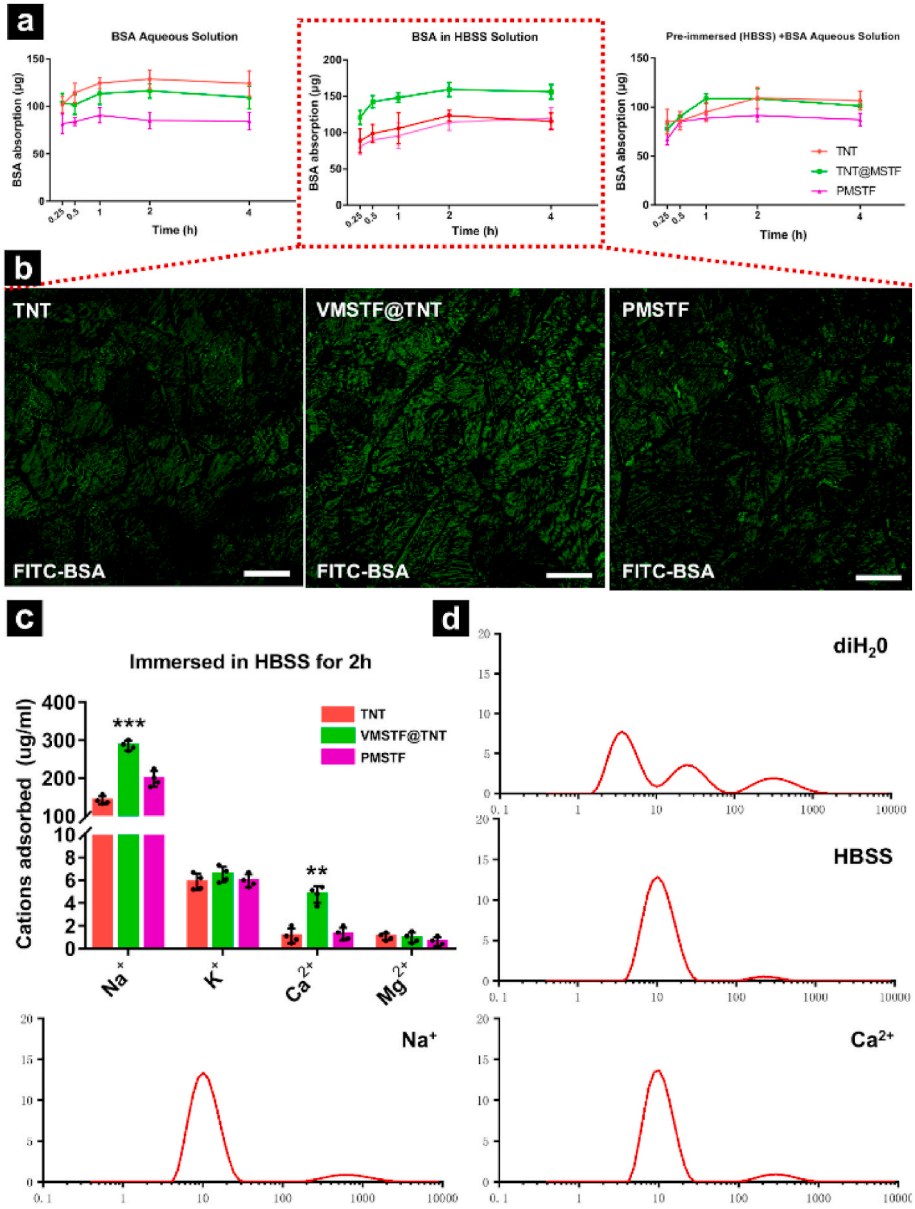

Fig. 8. The adsorption of BSA (a), FITC-BSA (b), and all cations from HBSS (c) on three samples. White scale bar = 200 μm. Together with the size distributions of BSA in different solutions from DLS measurements (d), the concentrations of Na^+, Ca^{2+} are equal to their contents in HBSS. **p < 0.01, ***p < 0.001 (VS TNT, PMSTF).

$2\ (—SiOH) + Ca^{2+} \rightarrow (—SiO)_2Ca + 2H^+$ [62]

$(—SiOH) + Na^+ \rightarrow (—SiO)\ Na + H^+$ [63].

More importantly, Na^+ and Ca^{2+} can also exert a significant electrostatic effect with BSA [64,65] and were almost equivalent to HBSS, which can be indicated by the changes of hydrated particle size of BSA (Fig. 8d). The above results preliminarily prove our previous hypothesis.

The excellent protein adsorption capacity will facilitate the biomaterial to form a stronger protein layer, providing a more ideal adhesion microenvironment [66]. Therefore, we extended the observation time window (24 h) to evaluate the final effect of MC3T3-E1 attachment. The FE-SEM results (Fig. 9a) showed that after incubating for 24 h, all samples appeared the TNT morphology. However, the MC3T3-E1 cells on the surface of VMSTF@TNT were obviously extended, and a large number of lamellipodia can be find (Insets of Fig. 9a). More importantly, The filopodia on the surface of VMSTF@TNT were robust, and increased tiny protrusions from the lateral side were linked with the nanotubes (Red triangles in Fig. 9a). This result indicates that the presence of VMSTF can promote the adaptation and colonization of cells to substrate. Furthermore, VMSTF@TNT still maintained a higher attached cell number after 24 h, which is not surprising (Fig. 9c). But it was interesting that the cells on VMSTF@TNT also exhibited stronger adhesion force (516 N), higher than TNT (304 pN) and PMSTF (427 pN) (Fig. 9b, d). It may attribute to the wider cell spreading area on VMSTF@TNT, which directly leads to the increase of focal adhesion

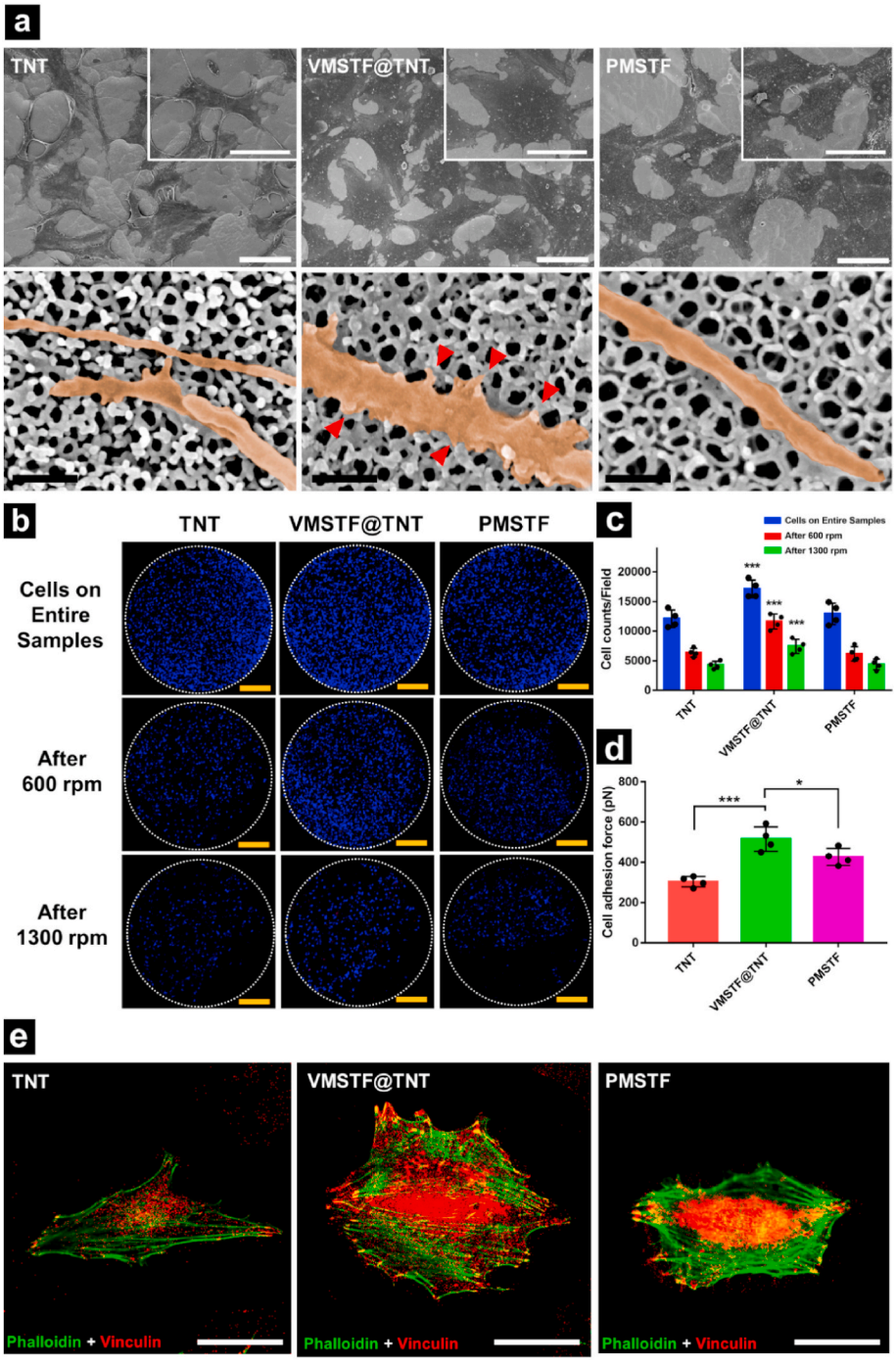

Fig. 9. Cell adhesion on three samples after incubating for 24 h. (a) Cell morphology and their filopodia observed by FE-SEM. The insets show the morphology of a single cell to compare the cell areas. The red triangles show the small lateral protrusions from the filopodia. (b) Confocal mosaic images of cell distributions on entire samples before and after being centrifuged at 600 rpm or 1300 rpm for 5 min. And the related cell counts (c) and cell adhesion forces (d) were also calculated. (e) The represent staining images of F-actin (green) and vinculin (red) on all samples. Black scale bar = 200 nm, white scale bar = 50 μm, yellow bar = 2 mm *p < 0.05, **p < 0.01, ***p < 0.001(VS TNT, PMSTF). (For interpretation of the references to color in this figure legend, the reader is referred to the Web version of this article.)

formation. This can be indicated by the vinculin staining, which is regard as an important component of focal adhesion (Fig. 9e) [67].

According to the above cell behaviors, the enhancement of osteoblasts responses by VMSTF coating may be attributed to the benefits of both Si element, the hydrophilicity surface and mesopore structure. It is reported that a proper concentration (<30 ppm) of aqueous Si is good for both osteoblasts proliferation and differentiation [68,69]. From the release data, our Si concentration in the supernatant was approximately in this range. The hydrophilic surface on one hand can enhance the adhesion and proliferation of osteoblasts [59]. To further prove this explanation, the cytotoxicity of HMSTF@TNT surface was also evaluated. The HMSTF@TNT was highly stable so that the Si release was very difficult. In addition, the water contact angle also increased after organic composition introduced. As a result, the cell viability was suppressed significantly (Fig. S10b). On the other hand, the vertical aligned mesochannels were proved to facilitate protein adsorption with the decisive participation of Na^{+} and Ca^{2+}. It may be attribute to the interactions between these ions with both Si–OH groups and proteins. In this study, VMSTF can be regarded as a buffer layer to achieve a faster cell adaptation to the material by promoting the formation of the protein layer. It provides cells with more adhesion sites, allows an earlier cell colonization, and may further accelerate subsequent cell behaviors (like proliferation and differentiation).

4. Conclusions

Our study has demonstrated a novel VMSTF coating strategy for Ti implant surface decoration. By altering the mesochannels perpendicular to substrate surface, the communication between mesochannels and external environment may be more effective and thus resulting in three main outstanding qualities: i) more rapid degradation that allows cell attachment with rigid Ti substrate as soon as possible; ii) capable of drug loading/release that can be gifted for therapy; iii) intrinsic promotion of osteoblasts adhesion and differentiation that can further enhance osteogenesis capacity of TNT. Taken together, these findings suggest that the VMSTF is a newly favorable versatile candidate for Ti implant surface coating, in order to achieve enhanced bioactivity.

CRediT authorship contribution statement

Zhe Li: Methodology, Validation, Investigation, Writing - original draft, Visualization. **Yide He:** Methodology, Validation, Investigation, Visualization. **Lasse Hyldgaard Klausen:** Methodology, Investigation. **Ning Yan:** Validation, Visualization. **Jing Liu:** Investigation. **Fanghao Chen:** Validation, Investigation. **Wen Song:** Writing - review & editing, Supervision, Funding acquisition. **Mingdong Dong:** Writing - review & editing, Supervision, Funding acquisition. **Yumei Zhang:** Supervision, Funding acquisition.

Declaration of competing interest

The authors declare no conflict of interest.

Acknowledgments

The work is granted by the National Natural Science Foundation of China [grant numbers 81530051, 31800790 and 31670966], Shaanxi Provincial Key Research and Development Plan Project (2019SF-031) and Young Talent fund of University Association for Science and Technology in Shaanxi, China (20190304). The work is also supported by Danmarks Frie Forskningsfond (9040-00219B) and Carlsbergfondet.

Appendix A. Supplementary data

Supplementary data to this article can be found online at https://doi.org/10.1016/j.bioactmat.2020.10.026.

References

[1] R. Shi, K. Hayashi, K. Ishikawa, Rapid osseointegration bestowed by carbonate apatite coating of rough titanium, Advanced Materials Interfaces 7 (18) (2020) 2000636.
[2] M. Saini, Y. Singh, P. Arora, V. Arora, K. Jain, Implant biomaterials: a comprehensive review. World journal of clinical cases: WJCC 3 (1) (2015) 52.
[3] Y. Liu, B. Rath, M. Tingart, J. Eschweiler, Role of implants surface modification in osseointegration: a systematic review, J. Biomed. Mater. Res. 108 (3) (2020) 470–484.
[4] L. Bai, Z. Du, J. Du, W. Yao, J. Zhang, Z. Weng, S. Liu, Y. Zhao, Y. Liu, X. Zhang, A multifaceted coating on titanium dictates osteoimmunomodulation and osteo/angio-genesis towards ameliorative osseointegration, Biomaterials 162 (2018) 154–169.
[5] Z. Chen, S. Ni, S. Han, R. Crawford, S. Lu, F. Wei, J. Chang, C. Wu, Y. Xiao, Nanoporous microstructures mediate osteogenesis by modulating the osteo-immune response of macrophages, Nanoscale 9 (2) (2017) 706–718.
[6] W. Zhang, H. Cao, X. Zhang, G. Li, Q. Chang, J. Zhao, Y. Qiao, X. Ding, G. Yang, X. Liu, A strontium-incorporated nanoporous titanium implant surface for rapid osseointegration, Nanoscale 8 (9) (2016) 5291–5301.
[7] A. Prasopthum, M. Cooper, K.M. Shakesheff, J. Yang, Three-dimensional printed scaffolds with controlled micro-/nanoporous surface topography direct chondrogenic and osteogenic differentiation of mesenchymal stem cells, ACS Appl. Mater. Interfaces 11 (21) (2019) 18896–18906.
[8] J. Wang, F. Meng, W. Song, J. Jin, Q. Ma, D. Fei, L. Fang, L. Chen, Q. Wang, Y. Zhang, Nanostructured titanium regulates osseointegration via influencing macrophage polarization in the osteogenic environment, Int. J. Nanomed. 13 (2018) 4029.
[9] Y. Dang, L. Zhang, W. Song, B. Chang, T. Han, Y. Zhang, L. Zhao, In vivo osseointegration of ti implants with a strontium-containing nanotubular coating, Int. J. Nanomed. 11 (2016) 1003.
[10] W. Song, C. Yang, D.Q. Svend Le, Y. Zhang, J. Kjems, Calcium–microrna complex-functionalized nanotubular implant surface for highly efficient transfection and enhanced osteogenesis of mesenchymal stem cells, ACS Appl. Mater. Interfaces 10 (9) (2018) 7756–7764.
[11] Y. Su, I. Cockerill, Y. Zheng, L. Tang, Y.-X. Qin, D. Zhu, Biofunctionalization of metallic implants by calcium phosphate coatings, Bioactive materials 4 (2019) 196–206.
[12] X.-Y. Yang, L.-H. Chen, Y. Li, J.C. Rooke, C. Sanchez, B.-L. Su, Hierarchically porous materials: synthesis strategies and structure design, Chem. Soc. Rev. 46 (2) (2017) 481–558.
[13] S.L. Suib, J. Přech, J. Čejka, Y. Kuwahara, K. Mori, H. Yamashita, Some novel porous materials for selective catalytic oxidations, Mater. Today 32 (2020) 244–259.
[14] S. Heo, J. Kim, G.K. Ong, D.J. Milliron, Template-free mesoporous electrochromic films on flexible substrates from tungsten oxide nanorods, Nano Lett. 17 (9) (2017) 5756–5761.
[15] W. Wu, L. Yu, Q. Jiang, M. Huo, H. Lin, L. Wang, Y. Chen, J. Shi, Enhanced tumor-specific disulfiram chemotherapy by in situ cu2+ chelation-initiated nontoxicity-to-toxicity transition, J. Am. Chem. Soc. 141 (29) (2019) 11531–11539.
[16] Y. Ding, Y. Fan, Y. Zhang, Y. He, S. Sun, H. Ma, Fabrication and optical sensing properties of mesoporous silica nanorod arrays, RSC Adv. 5 (110) (2015) 90659–90666.
[17] H. Qi, K.E. Shopsowitz, W.Y. Hamad, M.J. MacLachlan, Chiral nematic assemblies of silver nanoparticles in mesoporous silica thin films, J. Am. Chem. Soc. 133 (11) (2011) 3728–3731.
[18] G. Xu, X. Shen, L. Dai, Q. Ran, P. Ma, K. Cai, Reduced bacteria adhesion on octenidine loaded mesoporous silica nanoparticles coating on titanium substrates, Mater Sci Eng C Mater Biol Appl. 70 (PT.1) (2017) 386–395.
[19] J. Luo, X. Ding, W. Song, J.Y. Bai, J. Liu, Inducing macrophages M2 polarization by dexamethasone laden mesoporous silica nanoparticles from titanium implant surface for enhanced osteogenesis, Acta Metall. Sin. 32 (10) (2019) 75–82.
[20] N. Hao, L. Li, F. Tang, Shape matters when engineering mesoporous silica-based nanomedicines, Biomaterials science 4 (4) (2016) 575–591.
[21] K.-C. Kao, C.-H. Lin, T.-Y. Chen, Y.-H. Liu, C.-Y. Mou, A general method for growing large area mesoporous silica thin films on flat substrates with perpendicular nanochannels, J. Am. Chem. Soc. 137 (11) (2015) 3779–3782.
[22] M. Wan, J. Zhang, Q. Wang, S. Zhan, X. Chen, C. Mao, Y. Liu, J. Shen, In situ growth of mesoporous silica with drugs on titanium surface and its biomedical applications, ACS Appl. Mater. Interfaces 9 (22) (2017) 18609–18618.
[23] F. Yan, X. Lin, B. Su, Vertically ordered silica mesochannel films: electrochemistry and analytical applications, Analyst 141 (12) (2016) 3482–3495.
[24] T. Nasir, G. Herzog, M. Hébrant, C. Despas, L. Liu, A. Walcarius. Mesoporous silica thin films for improved electrochemical detection of paraquat, ACS Sens. 3 (2) (2018) 484–493.
[25] N. Vilà, E. André, R. Ciganda, J. Ruiz, D. Astruc, A. Walcarius, Molecular sieving with vertically aligned mesoporous silica films and electronic wiring through isolating nanochannels, Chem. Mater. 28 (8) (2016) 2511–2514.
[26] Y.-Q. Yeh, C.-Y. Tang, C.-Y. Mou, Two-dimensional crystals of mesoporous silica sba-15 nanosheets with perpendicular and open channels, Apl. Mater. 2 (11) (2014) 113303.
[27] K. Ariga, A. Vinu, Y. Yamauchi, Q. Ji, J.P. Hill, Nanoarchitectonics for mesoporous materials, Bull. Chem. Soc. Jpn. 85 (1) (2012) 1–32.
[28] A. Walcarius, E. Sibottier, M. Etienne, J. Ghanbaja, Electrochemically assisted self-assembly of mesoporous silica thin films, Nat. Mater. 6 (8) (2007) 602–608.

[29] M.-A. Pizzoccaro-Zilamy, C. Huiskes, E.G. Keim, S.N. Sluijter, H. van Veen, A. Nijmeijer, L. Winnubst, M.W. Luiten-Olieman, New generation of mesoporous silica membranes prepared by a stöber-solution pore-growth approach, ACS Appl. Mater. Interfaces 11 (20) (2019) 18528–18539.
[30] A. Stein, S.G. Rudisill, N.D. Petkovich, Perspective on the influence of interactions between hard and soft templates and precursors on morphology of hierarchically structured porous materials, Chem. Mater. 26 (1) (2014) 259–276.
[31] H. Gustafsson, S. Isaksson, A. Altskär, K. Holmberg, Mesoporous silica nanoparticles with controllable morphology prepared from oil-in-water emulsions, J. Colloid Interface Sci. 467 (2016) 253–260.
[32] L. Ernawati, R. Balgis, T. Ogi, K. Okuyama, Tunable synthesis of mesoporous silica particles with unique radially oriented pore structures from tetramethyl orthosilicate via oil–water emulsion process, Langmuir 33 (3) (2017) 783–790.
[33] Y. Liu, D. Shen, G. Chen, A.A. Elzatahry, M. Pal, H. Zhu, L. Wu, J. Lin, D. Al-Dahyan, W. Li, Mesoporous silica thin membranes with large vertical mesochannels for nanosize-based separation, Adv. Mater. 29 (35) (2017) 1702274.
[34] W. Song, M. Shi, M. Dong, Y. Zhang, Inducing temporal and reversible autophagy by nanotopography for potential control of cell differentiation, ACS Appl. Mater. Interfaces 8 (49) (2016) 33475–33483.
[35] Y. He, J. Luo, Y. Zhang, Z. Li, F. Chen, W. Song, Y. Zhang, The unique regulation of implant surface nanostructure on macrophages m1 polarization. Materials Science and Engineering: C. 106 (2020) 110221.
[36] X. Wang, L. Chen, Z. Teng, Z.-F. Wang, Facile method to efficiently fabricate large-size mesoporous organosilica nanosheets with uniform tunable pore size for robust separation membranes, Chem. Mater. 31 (10) (2019) 3823–3830.
[37] Y. Zhou, J.H. Schattka, M. Antonietti, Room-temperature ionic liquids as template to monolithic mesoporous silica with wormlike pores via a sol− gel nanocasting technique, Nano Lett. 4 (3) (2004) 477–481.
[38] J. Wu, Z. Mao, C. Gao, Controlling the migration behaviors of vascular smooth muscle cells by methoxy poly (ethylene glycol) brushes of different molecular weight and density, Biomaterials 33 (3) (2012) 810–820.
[39] K. Xu, W. Chen, G. Fu, X. Mou, R. Hou, Y. Zhu, K. Cai, In situ self-assembly of graphene oxide/polydopamine/sr2+ nanosheets on titanium surfaces for enhanced osteogenic differentiation of mesenchymal stem cells, Carbon 142 (2019) 567–579.
[40] L.K. Andersen, S.A. Contera, J. Justesen, M. Duch, O. Hansen, J. Chevallier, M. Foss, F.S. Pedersen, F. Besenbacher, Cell volume increase in murine mc3t3-e1 pre-osteoblasts attaching onto biocompatible tantalum observed by magnetic ac mode atomic force microscopy, Eur. Cell. Mater. 10 (61) (2005) 8.
[41] J. Yang, D. Shen, Y. Wei, W. Li, F. Zhang, B. Kong, S. Zhang, W. Teng, J. Fan, W. Zhang, Monodisperse core-shell structured magnetic mesoporous aluminosilicate nanospheres with large dendritic mesochannels, Nano Research 8 (8) (2015) 2503–2514.
[42] K. Wiercigroch-Walkosz, J. Cichos, M. Karbowiak, Growth of silica shell on hydrophobic upconverting nanocrystals–mechanism and control of porosity, Colloid. Surface. Physicochem. Eng. Aspect. 572 (2019) 1–9.
[43] F. Hou, W. Ding, W. Qu, A.O. Oladejo, F. Xiong, W. Zhang, R. He, H. Ma, Alkali solution extraction of rice residue protein isolates: influence of alkali concentration on protein functional, structural properties and lysinoalanine formation, Food Chem. 218 (2017) 207–215.
[44] J. Yang, G.-S. Lin, C.-Y. Mou, K.-L. Tung, Diatom-mimicking ultrahigh-flux mesoporous silica thin membrane with straight-through channels for selective protein and nanoparticle separations, Chem. Mater. 31 (5) (2019) 1745–1751.
[45] J. Wei, L. Zou, Synthesis of magnetical microspheres with tunable large pore mesostructures, J. Porous Mater. 23 (3) (2016) 577–581.
[46] J. Yang, G.-S. Lin, C.-Y. Mou, K.-L. Tung, Mesoporous silica thin membrane with tunable pore size for ultrahigh permeation and precise molecular separation, ACS Appl. Mater. Interfaces 12 (6) (2020) 7459–7465.
[47] X. Li, G. Qin, Y. Wang, W. Wei, Keggin-type phosphotungstic acid supported on mesoporous sio 2–al 2 o 3 aerogel like beads and their application in the isopropylation of naphthalene, J. Sol. Gel Sci. Technol. 72 (2) (2014) 405–414.
[48] M. Ebrahimi-Gatkash, H. Younesi, A. Shahbazi, A. Heidari, Amino-functionalized mesoporous mcm-41 silica as an efficient adsorbent for water treatment: batch and fixed-bed column adsorption of the nitrate anion, Applied Water Science 7 (4) (2017) 1887–1901.
[49] T.M. Albayati, I.K. Salih, H.F. Alazzawi, Synthesis and characterization of a modified surface of sba-15 mesoporous silica for a chloramphenicol drug delivery system, Heliyon 5 (10) (2019) e02539.
[50] B. Yang, Y. Chen, J. Shi, Mesoporous silica/organosilica nanoparticles: synthesis, biological effect and biomedical application, Mater. Sci. Eng. R Rep. 137 (2019) 66–105.
[51] M. Moritz, M. Geszke-Moritz, Mesoporous materials as multifunctional tools in biosciences: principles and applications, Mater. Sci. Eng. C 49 (2015) 114–151.
[52] D. Shen, J. Yang, X. Li, L. Zhou, R. Zhang, W. Li, L. Chen, R. Wang, F. Zhang, D. Zhao, Biphase stratification approach to three-dimensional dendritic biodegradable mesoporous silica nanospheres, Nano Lett. 14 (2) (2014) 923–932.
[53] N. Ma, Y. Deng, W. Liu, S. Li, J. Xu, Y. Qu, K. Gan, X. Sun, J. Yang, A one-step synthesis of hollow periodic mesoporous organosilica spheres with radially oriented mesochannels, Chem. Commun. 52 (17) (2016) 3544–3547.
[54] M.A. Wahab, J.N. Beltramini, Recent advances in hybrid periodic mesostructured organosilica materials: opportunities from fundamental to biomedical applications, RSC Adv. 5 (96) (2015) 79129–79151.
[55] X. Dereka, E. Calciolari, N. Donos, N. Mardas, Osseointegration in osteoporotic-like condition: a systematic review of preclinical studies, J. Periodontal. Res. 53 (6) (2018) 933–940.
[56] Q. Gan, J. Zhu, Y. Yuan, H. Liu, J. Qian, Y. Li, C. Liu, A dual-delivery system of ph-responsive chitosan-functionalized mesoporous silica nanoparticles bearing bmp-2 and dexamethasone for enhanced bone regeneration, J. Mater. Chem. B 3 (10) (2015) 2056–2066.
[57] I.A. Paun, M. Zamfirescu, C.R. Luculescu, A.M. Acasandrei, C.C. Mustaciosu, M. Mihailescu, M. Dinescu, Electrically responsive microreservoires for controllable delivery of dexamethasone in bone tissue engineering, Appl. Surf. Sci. 392 (2017) 321–331.
[58] Z.-C. Chiang, S.-H. Yu, A.-C. Chao, G.-C. Dong, Preparation and characterization of dexamethasone-immobilized chitosan scaffold, J. Biosci. Bioeng. 113 (5) (2012) 654–660.
[59] A. Hasan, S.K. Pattanayek, L.M. Pandey, Effect of functional groups of self-assembled monolayers on protein adsorption and initial cell adhesion, ACS Biomater. Sci. Eng. 4 (9) (2018) 3224–3233.
[60] B. Kasemo, Biological surface science, Surf. Sci. 500 (1–3) (2002) 656–677.
[61] A. Shamloo, M. Sarmadi, Investigation of the adhesive characteristics of polymer–protein systems through molecular dynamics simulation and their relation to cell adhesion and proliferation, Integrative Biology 8 (12) (2016) 1276–1295.
[62] T. Kawai, C. Ohtsuki, M. Kamitakahara, K. Hosoya, M. Tanihara, T. Miyazaki, Y. Sakaguchi, S. Konagaya, In vitro apatite formation on polyamide containing carboxyl groups modified with silanol groups, J. Mater. Sci. Mater. Med. 18 (6) (2007) 1037–1042.
[63] J.M. Rimsza, R.E. Jones, L.J. Criscenti, Interaction of naoh solutions with silica surfaces, J. Colloid Interface Sci. 516 (2018) 128–137.
[64] O. Becconi, E. Ahlstrand, A. Salis, R. Friedman, Protein-ion interactions: simulations of bovine serum albumin in physiological solutions of nacl, kcl and licl, Isr. J. Chem. 57 (5) (2017) 403–412.
[65] J. Gałęzowska, E. Chmielewska, Thermodynamics of the interactions of aminobisphosphonates and their calcium complexes with bovine serum albumin, Chem. Biodivers. 15 (10) (2018) e1800272.
[66] Z. Jia, W. Zhou, J. Yan, P. Xiong, H. Guo, Y. Cheng, Y. Zheng, Constructing multilayer silk protein/nanosilver biofunctionalized hierarchically structured 3d printed ti6al4 v scaffold for repair of infective bone defects, ACS Biomater. Sci. Eng. 5 (1) (2018) 244–261.
[67] Q. Ma, N. Jiang, S. Liang, F. Chen, L. Fang, X. Wang, J. Wang, L. Chen, Functionalization of a clustered tio 2 nanotubular surface with platelet derived growth factor-bb covalent modification enhances osteogenic differentiation of bone marrow mesenchymal stem cells, Biomaterials 230 (2020) 119650.
[68] Z. Chen, T. Klein, R.Z. Murray, R. Crawford, J. Chang, C. Wu, Y. Xiao, Osteoimmunomodulation for the development of advanced bone biomaterials, Mater. Today 19 (6) (2016) 304–321.
[69] A.M. Pietak, J.W. Reid, M.J. Stott, M. Sayer, Silicon substitution in the calcium phosphate bioceramics, Biomaterials 28 (28) (2007) 4023–4032.